

On the Interpretation of High Velocity White Dwarfs as Members of the Galactic Halo

P. Bergeron¹, María Teresa Ruiz², M. Hamuy³, S. K. Leggett⁴, M. J. Currie⁵,
C.-P. Lajoie¹, and P. Dufour¹

ABSTRACT

A detailed analysis of 32 of the 38 halo white dwarf candidates identified by Oppenheimer et al. is presented, based on model atmosphere fits to observed energy distributions built from optical *BVRI* and infrared *JHK* CCD photometry. Effective temperatures and atmospheric compositions are determined for all objects, as well as masses and cooling ages when trigonometric parallax measurements are available. This sample is combined with that of other halo white dwarf candidates and disk white dwarfs to study the nature of these objects in terms of reduced proper motion diagrams, tangential velocities, and stellar ages. We reaffirm the conclusions of an earlier analysis based on photographic magnitudes of the same sample that total stellar ages must be derived in order to associate a white dwarf with the old halo population, and that this can only be accomplished through precise mass and distance determinations.

Subject headings: Galaxy: halo — stars: fundamental parameters — stars: kinematics — stars: individual (LHS 1402, WD 2356–209) — white dwarfs

1. Introduction

White dwarf stars cool slowly enough that even the coolest and thus oldest white dwarfs are still visible (see Fontaine et al. 2001, for a review). The abrupt cutoff in the observed

¹Département de Physique, Université de Montréal, C.P. 6128, Succ. Centre-Ville, Montréal, Québec, Canada, H3C 3J7; bergeron,lajoie,dufour@astro.umontreal.ca.

²Departamento de Astronomía, Universidad de Chile, Casilla 36-D, Santiago, Chile; mtruiz@das.uchile.cl.

³Las Campanas Observatory, Carnegie Observatories, Casilla 601, La Serena, Chile; mhamuy@lco.cl.

⁴UKIRT, Joint Astronomy Centre, 660 North A'ohoku Place, Hilo, HI 96720; s.leggett@jach.hawaii.edu.

⁵Starlink Project, Rutherford Appleton Laboratory, Chilton, Didcot, Oxon OX11 0QX, UK; mjc@star.rl.ac.uk.

luminosity function of white dwarfs has been used by Winget et al. (1987) to infer the age of the local Galactic disk. A more recent determination by Leggett et al. (1998) using the 43 white dwarfs in the original sample of Liebert et al. (1988) lead to an age estimate of 8 ± 1.5 Gyr. White dwarf stars are also being used in globular clusters to get an independent estimate of the cluster ages (Hansen et al. 2004).

There has been a growing interest in identifying white dwarfs in the old halo population of our Galaxy, primarily to determine whether these old remnants could contribute significantly to the halo dark matter. Oppenheimer et al. (2001a, hereafter OHDHS) claimed to have discovered such a population by identifying 38 cool halo white dwarf candidates in the SuperCOSMOS Sky Survey, with an inferred space density that could account for 2% of the halo dark matter. The various criticisms that followed that study (see, e.g. Reid et al. 2001; Hansen 2001; Torres et al. 2002) were re-examined by Salim et al. (2004) who basically confirmed the conclusions reached by OHDHS. Most of these studies looked at these halo white dwarf candidates from the point of view of their kinematics.

Bergeron (2003) analyzed the photographic magnitudes obtained by OHDHS using model atmosphere fits to observed energy distributions following the photometric method described at length in Bergeron et al. (1997, hereafter BRL) and Bergeron et al. (2001, hereafter BLR). The analysis suggested that most of the white dwarfs in the OHDHS sample were probably too hot and too young to be associated with the halo population of the Galaxy. In this paper we present a similar analysis based on CCD photometry rather than photographic magnitudes, and with the addition of near-infrared photometry. Our photometric observations and theoretical framework are described respectively in § 2 and 3. The results of our analysis in terms of reduced proper motion diagrams, tangential velocities, and stellar ages are then presented in § 4. Our conclusions follow in § 5.

2. Photometric Observations

Optical *BVRI* CCD photometry has been secured for 30 white dwarfs taken from the OHDHS sample during several runs in 2002 and 2003, at Las Campanas (Carnegie Observatories) using the 1.3 m Warsaw telescope and the 1 m Swope telescope. Photometric standards from Landolt (1983) were used for calibration. Our photometry is reported in Table 1 together with the number of independent observations (N) for each object. Uncertainties are approximately 5% at B and 3% at VRI . For the two stars with $N = 0$, we have used the photographic magnitudes of OHDHS transformed into the standard V and I magnitudes using the relations defined in equations (1) to (5) of Salim et al. (2004). Our optical photometry is compared in Figure 1 with that of Salim et al. (2004, their Table 2).

The agreement between both photometric sets is excellent. The largest discrepancy is for the V magnitude of WD 0205–053¹ for which Salim et al. report a value 0.31 mag fainter than our measurement, with an uncertainty of 0.145 mag.

The infrared JHK photometry for 22 of the white dwarfs in Table 1 was obtained between 2002 September 23 and 26 using ClassicCam on Magellan. Four more stars were also observed at Las Campanas using the Dupont (100-inch) telescope and the WIRC camera, on 2003 December 14 and 15. One other was observed on the UK Infrared Telescope (UKIRT) using the UFTI camera, on 2004 June 26. These observations were calibrated using either the photometric standards of Persson et al. (1998) or Hawarden et al. (2001). The ClassicCam data were reduced using the software described in Currie & Cavanagh (2004). Infrared data for LHS 147 and LHS 542 are taken from BLR, and for LHS 4033 from Dahn et al. (2004). Out of the 32 objects listed in Table 1, 22 have JHK measurements, 8 only have J and H , while 2 have no infrared data. Also reported in Table 1 are the infrared photometric uncertainties (in parentheses) and the number of independent observations.

3. Theoretical Framework

The model atmospheres used in this analysis are described at length in Bergeron et al. (1995a, see also BRL and BLR) with the collision-induced opacities from molecular hydrogen updated from the work of Jørgensen et al. (2000) and Borysow et al. (2001). These models are in local thermodynamic equilibrium, they allow energy transport by convection, and they can be calculated with arbitrary mixed hydrogen and helium compositions.

Synthetic colors² are obtained using the procedure outlined in Bergeron et al. (1995b) but with the new Vega fluxes taken from Bohlin & Gilliland (2004) and the Vega magnitudes from Table A1 of Bessell et al. (1998). Similarly, in order to compare the photometric observations with the model atmosphere predictions, we convert (see also BRL) the optical and infrared magnitudes m into observed fluxes averaged over the transmission function $S_m(\lambda)$ using the following equation

¹Here and in the following we use for consistency the object names as defined in OHDHS. Note, however, that when OHDHS assigned a WD number to an object, it was based on 2000 coordinates while it would have been more appropriate to use the 1950 coordinates following the rules of the white dwarf catalog of McCook & Sion (1999). The correct WD numbers are used in the WD column of our Table 1.

²These synthetic colors can be obtained at <http://www.astro.umontreal.ca/~bergeron/CoolingModels>

$$m = -2.5 \log f_\lambda^m + c_m , \quad (1)$$

where

$$f_\lambda^m = \frac{\int_0^\infty f_\lambda S_m(\lambda) d\lambda}{\int_0^\infty S_m(\lambda) d\lambda} \quad (2)$$

is the averaged observed flux received at Earth. The transmission functions $S_m(\lambda)$ are taken from Bessell (1990) for the *BVRI* filters on the Johnson-Cousins photometric system, and from Bessell & Brett (1988) for the *JHK* filters on the Johnson-Glass system. The constants c_m for each passband using the new fluxes and zero points for Vega are $c_B = -20.4761$, $c_V = -21.0798$, $c_R = -21.6300$, $c_I = -22.3480$, $c_J = -23.7417$, $c_H = -24.8387$, and $c_K = -25.9877$. These constants differ slightly from those used by BRL and BLR, which were based on older Vega fluxes. Note also that with this new calibration, the +0.05 mag correction determined empirically and applied by BRL to the *J*, *H*, and *K* constants is not required here (see § 5.2.1 of BRL).

Since some of our observed magnitudes were obtained on the infrared system defined by Persson et al. (1998), we also calculated theoretical colors using the filter passbands described in their Appendix, but found negligible differences with the calculations using the Johnson-Glass system. We thus rely only on the latter in our analysis.

4. Results

4.1. Two-color Diagrams

We first present in Figure 2 the (*V*–*I*, *V*–*H*) two-color diagram for 29 objects from Table 1. Spectroscopic observations obtained from B. R. Oppenheimer (2004, private communication) are used to discriminate between DA (i.e. spectra showing H α) and non-DA stars. Also shown are the theoretical colors for our pure hydrogen, pure helium, and $N(\text{H})/N(\text{He}) = 10^{-5}$ model atmospheres. The loops observed in this diagram for the models containing hydrogen are the result of the presence of the collision-induced opacity from molecular hydrogen that reduces the flux significantly in the infrared. The effect occurs at higher effective temperature in the models at $N(\text{H})/N(\text{He}) = 10^{-5}$ because despite the fact that the abundance of hydrogen is greatly reduced, the higher atmospheric pressure of these models increases the number of collisions, which in turn increases the contribution of the H₂-He collision-induced opacity. Smaller or larger hydrogen abundances would yield smaller infrared flux deficiencies according to the calculations of Bergeron & Leggett (2002, see their Fig. 5).

DA stars (filled circles) follow nicely the hydrogen sequence. Since the pure hydrogen and pure helium sequences start at $T_{\text{eff}} = 12,000$ K, the location of the hottest DA stars in Figure 2 already suggests that several stars in the OHDHS sample are very hot. One non-DA star overlapping the DA stars, LHS 1447, is warm enough to show $\text{H}\alpha$ according to its location in Figure 2, a result that suggests it probably has a helium-rich atmospheric composition. At lower effective temperatures, $T_{\text{eff}} < 5000$ K, $\text{H}\alpha$ disappears altogether — even in pure hydrogen atmospheres — because of the Boltzmann factor. Hence we can no longer rely on the presence of $\text{H}\alpha$ to infer the atmospheric composition of the white dwarf and fits to the energy distribution must be used instead, as discussed in the BRL and BLR analyses. As can be seen from Figure 2, the pure hydrogen and pure helium sequences cross each other at low temperatures, which makes the discrimination between both atmospheric compositions a difficult task. This problem is less severe when the entire energy distribution is used, however (see below).

Two objects are labeled in Figure 2: WD 2356–209, further discussed in §4.2.1, is a cool white dwarf with an odd spectrum according to OHDHS, with a strong absorption feature near 6000 \AA that strongly affects the V magnitude in Figure 2. LHS 1402, further discussed in §4.2.2, is another extremely cool white dwarf candidate showing a very strong infrared flux deficiency similar to those observed in LHS 3250 and SDSS 1337+00, or in the handful of candidates identified by Gates et al. (2004). As for LHS 3250 and SDSS 1337+00, the location of LHS 1402 in the $(V-I, V-H)$ two-color diagram suggests either an extremely cool hydrogen-atmosphere white dwarf, or a much warmer star with a helium-rich atmospheric composition.

4.2. Energy Distributions

To derive the atmospheric parameters for each star in our sample, we rely on the technique developed by BRL, which we briefly describe again here for completeness. To make use of all the photometric measurements simultaneously, we convert the magnitudes into observed fluxes using equation (1), and compare the resulting energy distributions with those predicted from our model atmosphere calculations. For each star, we obtain a set of seven (or less) average fluxes f_{λ}^m which can now be compared with the model fluxes. These model fluxes are also averaged over the filter bandpasses by substituting f_{λ} in equation (2) for the monochromatic Eddington flux H_{λ} . The average observed fluxes f_{λ}^m and model fluxes H_{λ}^m — which depend on T_{eff} , $\log g$, and $N(\text{He})/N(\text{H})$ — are related by the equation

$$f_{\lambda}^m = 4\pi (R/D)^2 H_{\lambda}^m, \quad (3)$$

where R/D is the ratio of the radius of the star to its distance from Earth. Our fitting procedure relies on the nonlinear least-squares method of Levenberg-Marquardt, which is based on a steepest descent method. The value of χ^2 is taken as the sum over all bandpasses of the difference between both sides of equation (3), properly weighted by the corresponding observational uncertainties. In our fitting procedure, we consider only T_{eff} and the solid angle free parameters.

As discussed by BRL, the energy distributions are not sensitive enough to surface gravity to constrain the value of $\log g$, and thus for white dwarfs with no parallax measurement, we simply assume $\log g = 8.0$. For stars with known trigonometric parallax measurements, we start with $\log g = 8.0$ and determine T_{eff} and $(R/D)^2$, which combined with the distance D obtained from the trigonometric parallax measurement yields directly the radius of the star R . The radius is then converted into mass using the cooling sequences described in BLR with thin and thick hydrogen layers, which are based on the calculations of Fontaine et al. (2001). In general, the $\log g$ value obtained from the inferred mass and radius will be different from our initial guess of $\log g = 8.0$, and the fitting procedure is thus repeated until an internal consistency in $\log g$ is reached.

Only three objects in our sample have trigonometric parallax measurements, LHS 147 (14.0 ± 9.2 mas), LHS 542 (32.2 ± 3.7 mas), and LHS 4033 (33.9 ± 0.6 mas). The value for LHS 4033 is taken from Dahn et al. (2004), while the values for the other stars correspond to much older measurements with corresponding larger uncertainties. We note that the uncertainty for LHS 147 is as much as 65 %. More modern unpublished measurements obtained by the US Naval Observatories indicate that the above values have not changed significantly, but the uncertainties have been greatly reduced (H. C. Harris, 2004, private communication).

Sample fits for four objects in our sample are displayed in Figure 3. The left panels compare our best solutions with pure hydrogen and pure helium atmospheric compositions, while the right panels show the observed spectra obtained by OHDHS near the $H\alpha$ region together with the model spectrum calculated from the pure hydrogen solution. Together, the left and right panels can be used to determine the atmospheric composition and effective temperature of each star. We explore here only pure hydrogen and pure helium atmospheric compositions; limits on traces of hydrogen or helium in cool white dwarf atmospheres have been discussed in BRL. Note that because the stars in the OHDHS sample are much fainter than those studied in BRL and BLR, the quality of the fits to the energy distributions are not as good.

WD 0100–645 represents a good example of a pure hydrogen atmosphere white dwarf. Even though the hydrogen ($\chi^2 = 4.0$) and helium ($\chi^2 = 5.3$) fits do not differ much, the presence of the $H\alpha$ feature clearly favors the hydrogen solution. The inferred effective tem-

perature is also consistent with the observed $H\alpha$ line profile. We note, however, that the predicted flux at I is outside the 1σ observational uncertainty with the hydrogen fit, suggesting that the measured flux at I may be in error. This emphasizes the importance of using the complete $BVRI$ and JHK energy distributions to study these faint objects instead of using color-color diagrams, which tend to accentuate these errors in the photometric measurements.

The second object in Figure 3, LHS 1447, is a good example of a pure helium atmosphere white dwarf. In this case, the χ^2 value of the helium fit (5.9) is much smaller than that of the hydrogen fit (23.7). In particular, the hydrogen model fails to reproduce the flux in the H bandpass within the uncertainties. This is related to the fact that the H^- opacity, which dominates in this temperature range, has a minimum at $1.6\ \mu\text{m}$ (bound-free threshold), producing a local maximum in the energy distribution of hydrogen models. Furthermore, the predicted $H\alpha$ line profile assuming a pure hydrogen atmosphere for LHS 1447 clearly rules out this solution.

The other two objects, F351–50 and WD 0227–444, are too cool to show $H\alpha$, even if we assume a pure hydrogen composition. Hence we must rely solely on the fits to the energy distributions. F351–50 represents an excellent example of a cool, pure hydrogen atmosphere white dwarf. The differences between the hydrogen and helium solutions are extreme in this case ($\chi^2 = 3.6$ for the hydrogen fit as opposed to ~ 150 for the helium fit). Our pure hydrogen fit, however, fails to reproduce the observed flux at B within the uncertainties, and also at V to a lesser extent. This discrepancy has been explained by BRL in terms of a missing opacity source in the ultraviolet of the pure hydrogen models, most likely due to a pseudo-continuum opacity originating from the Lyman edge (see § 5.2.2 of BRL for a complete description), although this explanation has been challenged by Wolff et al. (2002). Note also that the failure of the pure hydrogen models to match the observed fluxes in this particular region of the energy distribution is most likely at the origin of the peculiar solution obtained for F351–50 by Oppenheimer et al. (2001b) – $T_{\text{eff}} = 2844\ \text{K}$, $\log g = 6.5$, and $N(\text{He})/N(\text{H}) = 0$ (see their Fig. 9) – based solely on a spectrum covering the region between 0.4 and $1\ \mu\text{m}$.

Finally, WD 0227–444, shown at the bottom of Figure 3, represents a good example of a cool white dwarf with a pure helium atmosphere ($\chi^2 = 8.9$ as opposed to 25.1 for the hydrogen fit). In this case, only the observed flux at H is not matched by the helium model, within the uncertainties. In contrast, six out the seven bands used in our fitting procedure are not matched properly by the hydrogen model.

The atmospheric parameters T_{eff} , $\log g$, and atmospheric composition (H or He) for the 32 objects listed in Table 1 are given in Table 2 together with the calculated stellar mass,

absolute visual magnitude, luminosity, distance, and white dwarf cooling age. The latter is obtained from the theoretical cooling sequences described above. A value of $\log g = 8.0$ was assumed for all stars except where noted; photometric distances are given for these objects. Three objects in the OHDHS sample stood out in our analysis, WD 2356–209 and LHS 1402 labeled in Figure 2, which had to be analyzed in greater detail. We discuss them in the next two sections. The third object is the extremely massive DA white dwarf LHS 4033 analyzed in detail by Dahn et al. (2004).

4.2.1. *WD 2356–209*

WD 2356–209 whose spectrum is shown in Figure 2 of OHDHS and reproduced here in Figure 4, exhibits a strong absorption feature near 6000 Å, which has been interpreted by Salim et al. (2004) as possibly originating from an extremely broad Na I doublet. A similar object has also been reported by Harris et al. (2003, see SDSS J1330+6435 in their Fig. 10). Indeed, our modeling of the Na I D doublet in a helium-rich atmosphere matches the observed broadband energy distribution and the observed spectrum quite well (see Fig. 4). However, it was not possible to constrain effectively the sodium abundance in this object since variations in the sodium abundance could be compensated by changing the effective temperature (± 200 K for ± 1 dex in sodium abundances) with very little changes in the predicted spectrum in the wavelength range used here. Large differences are predicted shortward of 5000 Å, however, and high signal-to-noise spectroscopy in this region should help constrain better the abundances of sodium and other heavy elements in the atmosphere of WD 2356–209, as well as its effective temperature. Indeed, all the spectral features predicted in this region of the spectrum are sodium lines. For the moment, we adopt a solution with a sodium abundance close to the solar abundance, $N(\text{Na})/N(\text{He}) = 10^{-5}$ and $T_{\text{eff}} = 4790$ K, which produces enough blanketing in the optical to deplete the flux near the *B* filter. This abundance may seem extreme but nearly solar abundances of iron and magnesium have also been measured in the cool and massive DAZ star GD 362 (Gianninas et al. 2004).

4.2.2. *LHS 1402*

LHS 1402 whose spectrum is shown in Figure 2 of OHDHS and reproduced here in Figure 5, exhibits a strong infrared flux deficiency similar to those observed in LHS 3250 and SDSS 1337+00, and in the ultracool white dwarf candidates reported by Gates et al. (2004, their Fig. 2). The detailed photometric and model atmosphere analysis of the first two objects by Bergeron & Leggett (2002) has revealed that the infrared flux deficiency, steep optical

spectrum, and luminosity (known only for LHS 3250) could be explained better in terms of an extremely helium-rich atmospheric composition rather than a pure hydrogen composition. In the latter case, the infrared flux deficiency is the result of collision-induced absorptions by molecular hydrogen, a mechanism that becomes important only at very low temperatures when the collisions responsible for the absorption are between hydrogen molecules only. However, in a helium-rich environment, characterized by higher atmospheric pressures, collisions also occur with neutral helium. The overall result is that it is possible to reproduce the same infrared flux deficiency but at much higher effective temperatures and luminosities, in better agreement with the observations. Furthermore, the broad absorption feature near $0.8 \mu\text{m}$ predicted by the pure hydrogen models is simply not observed (see Fig. 7 of Bergeron & Leggett 2002).

This situation is similar for LHS 1402, as shown in Figure 5, where we contrast our best solutions for a pure hydrogen composition and a mixed hydrogen and helium composition. As for LHS 3250 and SDSS 1337+00, both solutions fail to reproduce adequately the peak of the energy distribution, although the helium-rich solution exhibits a broader peak, not as high as that of the hydrogen solution, in closer agreement with the observations. The reasons for this discrepancy is still being investigated by us and others (see, e.g., Kowalski & Saumon 2004). As discussed above, the dip near $0.8 \mu\text{m}$ predicted by the pure hydrogen solution is simply not observed, a result that suggests that the atmosphere of LHS 1402 is indeed helium rich. Since the effective temperatures inferred from both solutions differ by over 1000 K, a measurement of the trigonometric parallax and thus of the absolute visual magnitude should help discriminate between our two solutions, as was done for LHS 3250 by Bergeron & Leggett (2002, see their Fig. 8). In the following, we adopt the atmospheric parameters from our solution with $\log N(\text{H})/N(\text{He}) = -4.5$ shown in Figure 5. Note that the white dwarf cooling age obtained from the helium-rich solution, 9.86 Gyr given in Table 2, is significantly shorter than that derived from the hydrogen solution, 12.5 Gyr.

4.3. Reduced Proper Motion Diagram

One very important tool that is commonly used in identifying halo white dwarf candidates is the reduced proper motion diagram. The reduced proper motion combines an observed magnitude with the proper motion measurement to yield some estimate of the absolute magnitude of the star (see Knox et al. 1999). OHDHS and Bergeron (2003) relied on a reduced proper motion defined as $H_R = R_{59F} + 5 \log \mu + 5$, where R_{59F} is the photographic magnitude, and μ is the proper motion measured in arc seconds per year, and those values were plotted against the photographic color index $B_J - R_{59F}$. Stars that are relatively blue

and with large values of H_R in this diagram are viewed as good halo white dwarf candidates since old, and thus cool, white dwarfs have low luminosities and turn blue below ~ 3500 K. Moreover, white dwarfs belonging to different kinematic populations of the Galaxy will be well separated in this diagram.

Our improved reduced proper motion diagram using CCD photometric measurements is displayed in Figure 6 where the reduced proper motion $H_V = V + 5 \log \mu + 5$ is plotted against the $V-I$ color index. The open circles represent the data taken from the BRL and BLR samples, while the filled symbols correspond to the data taken from Table 1. The objects labeled in the Figure represent five of the six halo white dwarf candidates identified by Liebert et al. (1989) on the basis of their large tangential velocities. Two of these stars, LHS 147 and LHS 542, are in common with the OHDHS sample. The leftmost and rightmost objects in Figure 6 correspond to LHS 1402 and WD 2356–209, respectively, while the two stars at the bottom are the hydrogen-rich white dwarfs F351–50 and WD 0351–564, two of the coolest objects in Table 2.

Also differentiated in Figure 6 are the stars above and below $T_{\text{eff}} = 5000$ K. With the exception of LHS 1420, all stars below 5000 K (filled circles) overlap with the (extended) sequence defined by the disk sample of BRL and BLR. All stars to the left of this sequence have temperatures above 5000 K (filled diamonds). With the exception of LHS 542 at $T_{\text{eff}} = 4740$ K, all halo white dwarf candidates from Liebert et al. (1989) also have temperatures in excess of 5000 K. It thus appears that most objects identified in such reduced proper motion diagrams are not cool and old white dwarfs, but instead relatively hot white dwarfs with large proper motions, and presumably large tangential velocities (see next section). Even LHS 1402 appears relatively luminous for its blue $V-I$ color index, most likely because the infrared flux deficiency that characterizes its energy distribution is the result of H_2 -He collision-induced absorptions in a warm, helium-rich atmosphere, as opposed to H_2 - H_2 collision-induced absorptions in an extremely cool, hydrogen-rich atmosphere. Cool and old pure hydrogen atmosphere white dwarfs would reside at much larger values of the reduced proper motion.

4.4. Tangential Velocities

The kinematic analysis of Salim et al. (2004) in the $U - V$ plane velocities relies heavily on the distance estimates (see their Fig. 5 for instance). We compare in Figure 7 our own distance estimates with those given in Table 4 of Salim et al. Surprisingly, despite the much cruder approach used by Salim et al. to estimate individual distances, the results agree extremely well. The only noticeable exception is for LHS 4033 whose trigonometric parallax

measurement implies a distance much closer and a mass much larger ($M = 1.34 M_{\odot}$) than that obtained under the assumption of $\log g = 8.0$. We thus conclude that the kinematic analysis of Salim et al. will not be affected by our results, and will thus not be repeated here. We simply reaffirm the conclusions of Salim et al. that the kinematics in the U - and V -components of the velocity plane of the OHDHS sample are consistent with a mixed of thick-disk and halo white dwarfs.

We look instead at the distribution of tangential velocities v_{tan} with absolute visual magnitudes M_V for the OHDHS sample, displayed in Figure 8. The tangential velocities are calculated using the proper motions provided in Table 4 of Salim et al. (2004) and the distances taken here from Table 2. Also shown are the results for the trigonometric parallax sample of BLR, which includes three of the five halo white dwarf candidates from Liebert et al. (1989) labeled in Figure 8; LHS 282 and LHS 291 have trigonometric parallax measurements that are too uncertain to derive meaningful distances. LHS 147 and LHS 542 in common between the BLR and OHDHS samples demonstrate the repeatability of our atmospheric parameter measurements. The object at the very bottom is the massive white dwarf ESO 439–26 with an estimated mass of $\sim 1.2 M_{\odot}$, an effective temperature of 4500 K, and an absolute visual magnitude of $M_V=17.46$.

It is already clear that the tangential velocities of the OHDHS sample differ quite markedly from those of the disk stars. And indeed some objects have tangential velocities well in excess of 200 km s^{-1} . The most extreme case is for WD 0135–039 with a value of $v_{\text{tan}} = 430 \text{ km s}^{-1}$. This object is not particularly cool, however, with a temperature of 7470 K. Again we note that none of these objects are particularly cool (the right axis indicates the temperature scale for $0.6 M_{\odot}$ white dwarf models). Even the coolest object in our analysis, LHS 1402, has the smallest tangential velocities of all ($v_{\text{tan}} = 60 \text{ km s}^{-1}$). The objects with the largest tangential velocities even have tendencies to be located hotter than 7000 K, the three exceptions being LHS 542, WD 0351–564, and F351–50.

4.5. Stellar Ages

Insight into the nature of the halo white dwarf candidates identified by OHDHS may be gained by estimating their total stellar ages. Halo white dwarfs should have total ages well in excess of 10 Gyr. We show in Figure 9 the location in a mass versus effective temperature diagram of all white dwarfs taken from the parallax sample of BLR (open symbols) and the OHDHS sample (filled symbols). Various symbols explained in the legend are used to differentiate ranges of tangential velocities. White dwarfs from the OHDHS sample with no trigonometric parallax measurements and for which it is not possible to determine the mass

are shown at the bottom of the Figure.

Mass uncertainties are also indicated for all white dwarfs in the OHDHS sample with measured parallaxes (LHS 147, LHS 542, and LHS 4033) and for the white dwarfs in the BLR sample with $v_{\text{tan}} > 200 \text{ km s}^{-1}$ (LHS 56, LHS 147, and LHS 542; the last two objects are in common with the OHDHS sample and they have identical error bars). Unfortunately, these mass uncertainties are fairly large, with the exception of LHS 4033 at $M \sim 1.3 M_{\odot}$, which corresponds to a modern parallax measurement (Dahn et al. 2004). As discussed in § 4.2, however, both LHS 147 and LHS 542 have been measured with comparable accuracy, and the parallax values have not changed significantly from those used in Figure 9 (H. C. Harris, 2004, private communication).

Also superposed on this plot are the theoretical isochrones from the white dwarf cooling sequences discussed above with C/O-cores, $q(\text{He}) \equiv M_{\text{He}}/M_{\star} = 10^{-2}$, and $q(\text{H}) = 10^{-4}$. The solid lines represent the white dwarf cooling ages only. These parabola-shaped isochrones are the result of the onset of crystallization occurring first in the higher mass models, reducing the cooling timescales considerably. With decreasing effective temperature, crystallization gradually occurs in lower mass models, and the turning point of these parabola moves slowly towards lower masses. Since *total stellar ages* and not white dwarf cooling ages are the crucial aspect we want to investigate here, we must take into account the time spent on the main sequence. To do so, we follow the procedure outlined in Wood (1992) and we add to the white dwarf cooling age the main sequence lifetime t_{MS} calculated as $t_{\text{MS}} = 10(M_{\text{MS}}/M_{\odot})^{-2.5}$ Gyr where M_{MS} is the mass on the main sequence of the white dwarf progenitor. The latter is obtained from the initial-final mass relation for white dwarfs, a relation that is not particularly well determined, especially at low mass (see Weidemann 2000, for a review). Here we use the parameterization used by Wood (1992)

$$M_{\text{WD}} = A_{\text{IF}} \exp(B_{\text{IF}} M_{\text{MS}}) , \quad (4)$$

where M_{WD} is the mass of the white dwarf, and A_{IF} and B_{IF} represent constants that need to be determined empirically. Wood (1992) used the spectroscopic mass distribution of DA white dwarfs obtained by Bergeron et al. (1992) and derived $A_{\text{IF}} = 0.4$ and $B_{\text{IF}} = 0.125$. The mass distribution of Bergeron et al. relied on thin hydrogen layer models, while thick hydrogen models yield larger masses (Bragaglia, Renzini, & Bergeron 1995). Since the weight of evidence now is that most DA white dwarfs have thick outer hydrogen layers, we redetermined the constants in equation (4) by using the mass distribution obtained for the 348 DA stars from the Palomar-Green survey sample (Liebert et al. 2005), which is based on the thick hydrogen evolutionary models of Wood (1995). We obtain the following

constants, $A_{\text{IF}} = 0.45$ and $B_{\text{IF}} = 0.144$. Thus a main sequence star with a 12 Gyr lifetime – corresponding to a mass of $0.93 M_{\odot}$ – would produce a $0.51 M_{\odot}$ white dwarf remnant.

The above empirical initial-final mass relation has been derived using white dwarfs from the thin disk, while the relation for halo white dwarfs — which is even more poorly known — is probably similar to that of globular clusters. As discussed by Renzini et al. (1996), the mass of the white dwarfs currently being formed in globular clusters can be constrained by the luminosities of the red giant branch tip, the horizontal branch, the AGB termination, and the post-AGB stars, all of which are sensitive to the mass of the hydrogen exhausted core. All observations point to values between $M_{\text{WD}} = 0.51$ and $0.55 M_{\odot}$, virtually independent of metallicity (Renzini & Fusi Pecci 1988). Hence it is reasonable to assume that white dwarfs currently being formed in the halo should have masses in the same range. The empirical initial-final mass relation we derived above is certainly consistent with these results, although it should be considered a good approximation at best, and white dwarfs currently being formed in the halo could still be as massive as $0.55 M_{\odot}$.

The isochrones representing the white dwarf cooling ages plus main sequence ages using the initial-final mass relation described above are reproduced in Figure 9. It is clear that the total age of a white dwarf is strongly mass-dependent, a result which stresses the importance of determining reliable masses through precise trigonometric parallax measurements. For instance, all white dwarfs with masses below $M \lesssim 0.5 M_{\odot}$ cannot have been formed within the lifetime of the Galaxy, and they must be the result of common envelope evolution. Alternatively, these could be unresolved degenerate binaries, and their overluminosity would be wrongly interpreted here as single white dwarfs with large radii and low masses (see BRL and BLR for further discussion). Also, the results of Figure 9 illustrate how a 12 Gyr old white dwarf, say, could be found at any effective temperature, as long as its mass is precisely on the horizontal part of the isochrones near $\sim 0.5 M_{\odot}$, implying that it has recently (a few Gyr) evolved from a main sequence star slightly below $\sim 1 M_{\odot}$ (see discussion above).

Only three white dwarfs from the OHDHS sample have trigonometric parallax measurements. One of them is the extremely massive white dwarf LHS 4033 (Dahn et al. 2004) seen in the upper left corner of Figure 9. So not only this star does not have the proper kinematics to be associated with the halo population, but it is also much too young ($\tau < 2$ Gyr). The other two objects, LHS 147 and LHS 542, have more normal masses of $M = 0.64$ and $0.67 M_{\odot}$, respectively. Taken at face value, they both appear too young to be associated with the halo population, despite their halo kinematics. However, when the mass uncertainties are taken into account, their total stellar ages could be made consistent with the age of the halo. This stresses the importance of reducing the size of the parallax measurements through the use of modern CCD techniques, such as those currently being obtained at the USNO.

If the values of the trigonometric parallax measurements for LHS 147 and LHS 542 are confirmed, these two white dwarfs could indeed be very young according to our results. This conclusion seems to be independent of the particular choice of the initial-final mass relation adopted here since both stars have inferred masses nearly $0.1 M_{\odot}$ above the upper limit of $0.55 M_{\odot}$ for the white dwarfs currently being formed in globular clusters, and presumably in the galactic halo as well.

5. Conclusions

In this paper, we have demonstrated the importance of determining *total* stellar ages in order to associate any white dwarf with a given population. This can only be accomplished through a precise mass determination, which for cool white dwarfs require accurate trigonometric parallax measurements. Even though it is not possible to conclude at this stage that any white dwarf in the OHDHS sample is too young to belong to the halo population, with the glaring exception of LHS 4033, modern parallax measurements for at least two white dwarfs, LHS 147 and LHS 542, seem to indicate that young white dwarfs with halo kinematics do exist. The possibility that that young high velocity white dwarfs, most likely associated with the young disk, might exist is intriguing. Bergeron (2003) summarized some physical mechanisms proposed in the literature that could produce these young high-velocity white dwarfs. These include remnants of donor stars from close mass-transfer binaries that produced type Ia supernovae via the single degenerate channel (Hansen 2002), or other alternative mechanisms by which stars can be ejected from the thin disk into the galactic halo with the required high velocities.

The other white dwarf stars in the OHDHS sample are fairly warm, and the only way they could be associated with the halo population is to have stellar masses near $\sim 0.51 M_{\odot}$, in which case they can indeed be very old. Trigonometric parallaxes will hopefully become available for all stars from this sample in the near future. The two most likely halo candidates in the OHDHS sample are F351–50 and WD 0351–564 (the two objects at the bottom of Fig. 6 and also labeled in Fig. 8). They correspond to the two coolest objects in Figure 9 with $v_{\text{tan}} > 200 \text{ km s}^{-1}$ (the two rightmost filled circles at the bottom of the figure). Masses below $0.6 M_{\odot}$ would yield total stellar ages above 11 Gyr.

Based on the results of our analysis, we feel that any determination of the space density of white dwarfs in the halo or even in the thick disk based solely on a kinematic analysis is basically flawed, and one must combine such analyses with a precise determination of total stellar ages, which implies in turn that distance estimates must also be obtained (see, e.g. Pauli et al. 2005). Similarly, analyses based on reduced proper motion diagrams are likely to

reveal more of these young high-velocity white dwarfs rather than the long sought old white dwarf halo population.

We thank B. R. Oppenheimer for providing us with his spectroscopic observations. This work was supported in part by the NSERC Canada and by the Fund FQRNT (Québec). MTR received partial support from Fondecyt (1010404) and FONDAP (15010003). Support for this work was also provided to MH by NASA through Hubble Fellowship grant HST-HF-01139.01A awarded by the Space Telescope Science Institute, which is operated by the Association of Universities for Research in Astronomy, Inc., for NASA, under contract NAS 5-26555. The United Kingdom Infrared Telescope is operated by the Joint Astronomy Centre on behalf of the U.K. Particle Physics and Astronomy Research Council.

REFERENCES

- Bergeron, P. 2003, ApJ, 586, 201
- Bergeron, P., & Leggett, S. K. 2002, ApJ, 580, 1070
- Bergeron, P., Leggett, S. K., & Ruiz, M. T. 2001, ApJS, 133, 413 (BLR)
- Bergeron, P., Ruiz, M. T., & Leggett, S. K. 1997, ApJS, 108, 339 (BRL)
- Bergeron, P., Saffer, R. A., & Liebert, J. 1992, ApJ, 394, 228
- Bergeron, P., Saumon, D., & Wesemael, F. 1995a, ApJ, 443, 764
- Bergeron, P., Wesemael, F., & Beauchamp, A. 1995b, PASP, 107, 1047
- Bessell, M. S. 1990, PASP, 102, 1181
- Bessell, M. S., & Brett, J. M. 1988, PASP, 100, 1134
- Bessell, M. S., Castelli, F., & Plez, B. 1998, A&A, 333, 231
- Bohlin, R. C., & Gilliland, R. L. 2004, AJ, 127, 3508
- Borysow, A., Jørgensen, U. G., & Fu, Y. 2001, J. Quant. Spec. Radiat. Transf., 68, 235
- Bragaglia, A., Renzini, A., & Bergeron, P. 1995, ApJ, 443, 735
- Currie, M. J., & Cavanagh, B. 2004, ORAC-DR - Imaging Data Reduction User Guide, Starlink User Note 232.8 ³
- Dahn, C. C., Bergeron, P., Liebert, J., Harris, H. C., Canzian, B., Leggett, S. K., & Boudreault, S. 2004, ApJ, 605, 400
- Fontaine, G., Brassard, P., & Bergeron, P. 2001, PASP, 113, 409
- Gates, E. et al. 2004, ApJ, 612, L129
- Gianninas, A., Dufour, P., & Bergeron, P. 2004, ApJ, 617, L57
- Hansen, B. M. S. 2001, ApJ, 558, L39
- Hansen, B. M. S. 2002, ApJ, 582, 915

³<http://www.starlink.ac.uk/star/docs/sun232.htx/sun232.html>

- Hansen, B. M. S. et al. 2004, *ApJS*, 155, 551
- Harris, H. C., et al. 2003, *AJ*, 126, 1023
- Hawarden, T. G., Leggett, S. K., Letawski, M. B., Ballantyne, D. R., & Casali, M. M. 2001, *MNRAS*, 325, 563
- Jørgensen, U. G., Hammer, D., Borysow, A., & Falkesgaard, J. 2000, *A&A*, 361, 283
- Knox, R. A., Hawkins, M. R. S., & Hambly, N. C. 1999, *MNRAS*, 306, 736
- Kowalski, P. M., & Saumon, D. 2004 *ApJ*, 607, 970
- Landolt, A. U. 1983, *AJ*, 88, 439
- Leggett, S. K., Ruiz, M. T., & Bergeron, P. 1998, *ApJ*, 497, 294
- Liebert, J., Bergeron, P., & Holberg, J. B. 2005, *ApJS*, 156, 47
- Liebert, J., Dahn, C. C., & Monet, D. G. 1988, *ApJ*, 332, 891
- Liebert, J., Dahn, C. C., & Monet, D. G. 1989, in *IAU Colloq. 114, White Dwarfs*, ed. G. Wegner (Berlin: Springer), 15
- McCook, G. P., & Sion, E. M. 1999, *ApJS*, 121, 1
- Oppenheimer, B. R., Hambly, N. C., Digby, A. P., Hodgkin, S. T., & Saumon, D. 2001a, *Science*, 292, 698 (OHDHS)
- Oppenheimer, B. R., Saumon, D., Hodgkin, S. T., Jameson, R. F., Hambly, N. C., Chabrier, G., Filipenko, A. V., Coil, A. L., & Brown, M. E. 2001b, *ApJ*, 550, 448
- Pauli, E.-M., Heber, U., Napiwotzki, R., Altmann, M., & Odenkirchen, M. 2005, in *14th European Workshop on White Dwarfs*, ASP Conf. Series, eds. D. Koester & S. Mohler, in press
- Persson, S. E., Murphy, D. C., Krzeminski, W., Roth, M., & Rieke, M. J. 1998, *AJ*, 116, 2475
- Reid, I. N., Sahu, K. C., & Hawley, S. L. 2001, *ApJ*, 559, 942
- Renzini, A. et al. 1996, *ApJ*, 465, L23
- Renzini, A., & Fusi Pecci, F. 1988, *ARA&A*, 26, 199

- Salim, S., Rich, R. M., Hansen, B. M., Koopmans, L. V. E., Oppenheimer, B. R., & Blandford, R. D. 2004, *ApJ*, 601, 1075
- Torres, S., García-Berro, E., Burkert, A., & Isern, J., 2002, *MNRAS*, 336, 971
- Weidemann, V. 2000, *A&A*, 363, 647
- Winget et al. 1987, *ApJ*, 315, L77
- Wolff, B., Koester, D., & Liebert, J. 2002, *A&A*, 385, 995
- Wood, M. A. 1992, *ApJ*, 386, 539
- Wood, M. A. 1995, in 9th European Workshop on White Dwarfs, NATO ASI Series, ed. D. Koester & K. Werner (Berlin: Springer), 41

Table 1. Optical^a and Infrared Photometric Measurements

WD ^b	Name	<i>B</i>	<i>V</i>	<i>R</i>	<i>I</i>	<i>N</i>	<i>J</i>	<i>H</i>	<i>K</i>	<i>N</i>
0011–399	J0014–3937	19.28	18.19	17.57	17.07	2	16.43 (0.03)	16.23 (0.02)	16.17 (0.03)	1
0041–286	WD 0044–284	21.02	19.87	19.21	18.70	1	18.15 (0.03)	17.99 (0.04)	...	1
0042–064	WD 0045–061	19.19	18.26	17.71	17.22	2	16.83 (0.02)	16.59 (0.02)	16.54 (0.04)	1
0042–337	F351–50	20.54	19.01	18.31	17.67	2	17.07 (0.02)	17.04 (0.03)	17.05 (0.05)	1
0058–647	WD 0100–645	17.77	17.37	17.14	16.78	1	16.57 (0.06)	16.40 (0.06)	16.34 (0.06)	1
0059–008	LP 586–51	18.40	18.18	18.18	18.07	1	18.27 (0.10)	18.30 (0.10)	...	1
0115–270	WD 0117–268	20.04	19.04	18.47	18.02	2	17.47 (0.02)	17.20 (0.03)	17.23 (0.10)	1
0120–280	WD 0123–278	20.93	19.96	19.41	18.90	1	18.29 (0.04)	18.09 (0.04)	18.05 (0.11)	1
0133–042	WD 0135–039	20.01	19.68	19.46	19.24	1	0
0133–548	WD 0135–546	19.44	18.37	17.79	17.29	1	16.67 (0.02)	16.44 (0.02)	16.40 (0.04)	1
0136–340	LHS 1274	17.59	17.18	16.88	16.65	1	16.44 (0.06)	16.25 (0.06)	16.12 (0.06)	1
0145–174	LHS 147	17.97	17.62	17.38	17.16	1	17.00 (0.05)	16.85 (0.05)	16.86 (0.05)	2
0151–016	WD 0153–014	18.90	18.69	18.57	18.51	1	18.29 (0.06)	18.29 (0.06)	...	1
0202–055	WD 0205–053	19.91	18.59	17.85	17.17	2	16.56 (0.03)	16.53 (0.03)	16.46 (0.04)	1
0212–420	WD 0214–419	20.80	19.81	19.33	18.64	1	18.28 (0.04)	18.03 (0.05)	...	1
0222–291	LHS 1402	18.73	18.05	18.06	18.49	2	19.09 (0.05)	19.43 (0.10)	...	1
0225–446	WD 0227–444	20.64	19.53	18.98	18.41	1	17.93 (0.04)	17.78 (0.04)	17.59 (0.07)	1
0246–302	LHS 1447	18.94	18.50	18.14	17.90	1	17.68 (0.06)	17.65 (0.06)	17.62 (0.10)	1
0304–074	LP 651–74	18.00	17.35	16.98	16.62	3	0
0338–331	WD 0340–330	21.07	19.76	19.19	18.65	2	17.88 (0.05)	17.71 (0.04)	17.62 (0.06)	1
0343–363	WD 0345–362	21.26	20.23	19.47	18.94	2	18.24 (0.05)	18.10 (0.04)	18.29 (0.10)	1
0350–566	WD 0351–564	22.11	20.56	19.72	18.89	1	18.44 (0.05)	18.47 (0.06)	...	1
2211–392	WD 2214–390	16.41	15.92	15.59	15.26	1	14.92 (0.02)	14.66 (0.02)	14.65 (0.04)	1
2239–199	WD 2242–197	20.65	19.74	19.24	18.87	1	18.35 (0.03)	18.08 (0.05)	...	1
2256–467	WD 2259–465	20.60	19.56	18.96	18.48	2	17.96 (0.03)	17.83 (0.03)	17.63 (0.08)	1
2316–064	LHS 542	19.23	18.15	17.53	16.99	1	16.38 (0.05)	16.12 (0.05)	16.08 (0.05)	2
2321–597	WD 2324–595	16.98	16.79	16.77	16.81	1	16.84 (0.02)	16.92 (0.03)	16.97 (0.05)	1
2343–481	WD 2346–478	...	17.95	...	17.11	0	16.43 (0.02)	16.17 (0.02)	16.06 (0.03)	1
2346–550	WD 2348–548	19.70	18.88	18.41	17.99	2	17.45 (0.03)	17.17 (0.03)	17.16 (0.06)	1
2349–031	LHS 4033	17.17	16.98	...	16.91	1	16.97 (0.05)	16.92 (0.05)	17.02 (0.05)	1
2352–326	LHS 4042	...	17.41	...	17.23	0	17.05 (0.02)	17.12 (0.03)	17.96 (0.10)	1
2354–211	WD 2356–209	21.24	21.03	19.92	18.78	2	18.33 (0.04)	18.28 (0.06)	...	1

^aOptical photometric uncertainties are 5% at *B* and 3% at *VRI*.

^bThe WD numbers are based on 1950 coordinates while those defined by OHDHS are based on 2000 coordinates.

Table 2. Atmospheric Parameters of Halo White Dwarf Candidates

WD	Name	T_{eff} (K)	$\log g^b$	Comp	M/M_{\odot}	M_V	D (pc)	v_{tan} (km s $^{-1}$)	Age ^a (Gyr)	Notes
0011–399	J0014-3937	4340 (70)	8.00	H	0.58	15.86	29	104	8.08	
0041–286	WD 0044–284	4770 (50)	8.00	He	0.57	15.44	77	134	6.57	
0042–064	WD 0045–061	5100 (50)	8.00	He	0.57	15.01	44	144	5.66	
0042–337	F351-50	4100 (60)	8.00	H	0.58	16.22	36	408	8.76	
0058–647	WD 0100–645	6900 (170)	8.00	H	0.59	13.64	55	145	1.57	1
0059–008	LP 586-51	10210 (600)	8.00	H	0.60	12.10	164	282	0.57	1
0115–270	WD 0117–268	4920 (50)	8.00	He	0.57	15.23	58	131	6.21	
0120–280	WD 0123–278	4880 (50)	8.00	He	0.57	15.27	86	149	6.29	
0133–042	WD 0135–039	7470 (350)	8.00	H	0.59	13.32	186	434	1.29	1
0133–548	WD 0135–546	4800 (40)	8.00	He	0.57	15.37	39	125	6.48	
0136–340	LHS 1274	7000 (180)	8.00	H	0.59	13.59	52	143	1.52	1
0145–174	LHS 147	7640 (180)	8.07	H	0.64	13.35	71	376	1.34	1, 2
0151–016	WD 0153–014	9000 (310)	8.00	H	0.60	12.59	166	317	0.79	1
0202–055	WD 0205–053	4170 (60)	8.00	H	0.58	16.19	30	147	8.56	
0212–420	WD 0214–419	4910 (60)	8.00	He	0.57	15.22	82	130	6.21	
0222–291	LHS 1402	3240 (70)	8.00	He	0.57	15.98	25	60	9.86	3
0225–446	WD 0227–444	4880 (50)	8.00	He	0.57	15.26	71	117	6.30	
0246–302	LHS 1447	6550 (170)	8.00	He	0.57	13.82	86	221	1.95	
0304–074	LP 651-74	5750 (190)	8.00	H	0.59	14.41	38	87	2.56	1
0338–331	WD 0340–330	4530 (160)	8.00	H	0.58	15.70	64	182	7.48	
0343–363	WD 0345–362	4230 (100)	8.00	H	0.58	16.10	66	191	8.42	
0350–566	WD 0351–564	3950 (90)	8.00	H	0.58	16.57	62	323	9.14	
2211–392	WD 2214–390	6290 (100)	8.00	H	0.59	14.03	23	121	1.98	1
2239–199	WD 2242–197	5400 (120)	8.00	H	0.58	14.79	97	162	3.61	1
2256–467	WD 2259–465	4940 (50)	8.00	He	0.57	15.20	74	152	6.15	
2316–064	LHS 542	4740 (50)	8.15	He	0.67	15.69	31	250	7.29	2
2321–597	WD 2324–595	11180 (330)	8.00	H	0.60	11.84	97	272	0.45	1
2343–481	WD 2346–478	4590 (120)	8.00	H	0.58	15.38	32	81	7.28	1
2346–550	WD 2348–548	5350 (100)	8.00	H	0.58	14.83	64	115	3.87	
2349–031	LHS 4033	10870 (370)	9.42	H	1.34	14.63	29	97	1.75	1, 2
2352–326	LHS 4042	9580 (230)	8.00	H	0.60	12.39	100	202	0.68	1
2354–211	WD 2356–209	4790 (50)	8.00	He	0.57	16.59	77	143	6.52	4

^aWhite dwarf cooling age only, not including the main sequence lifetime.

^bAssumed $\log g = 8$ except for stars with note (2).

Note. — (1) H α detected spectroscopically; (2) $\log g$ value inferred from the trigonometric parallax; (3) Solution obtained with a mixed hydrogen and helium composition; (4) Solution obtained with $N(\text{Na})/N(\text{He}) = 10^{-5}$ and strong absorption feature at V (see § 4.2.1).

Fig. 1.— Comparison of the optical *BVRI* photometry of Salim et al. (2004) with that obtained in this study.

Fig. 2.— (*V-I*, *V-H*) two-color diagram for the data set from Table 1; DA and non-DA stars are represented by filled and open circles, respectively, and the cross indicates the size of the average error bars. The objects marked are discussed in the text. Theoretical colors at $\log g = 8.0$ for models with pure hydrogen, pure helium, and $N(\text{H})/N(\text{He}) = 10^{-5}$ atmospheric compositions are also shown. The small dots on each sequence indicate values of T_{eff} from 3000 to 4500 K by steps of 500 K (from 3500 K only for the pure helium sequence); the sequences start below the middle of the plot at 12,000 K.

Fig. 3.— Left panels: Sample fits to the energy distributions of halo white dwarf candidates with pure hydrogen models (*filled circles*) and pure helium models (*open circles*); a value of $\log g = 8.0$ is assumed for all stars. The *BVRI* and *JHK* photometric observations are represented by error bars. Right panels: Normalized spectra near $\text{H}\alpha$ together with the synthetic line profiles interpolated at the parameters obtained from the energy distribution fits assuming a pure hydrogen atmospheric composition.

Fig. 4.— Our best fit to the energy distribution and optical spectrum of WD 2356–209. The *BVRI* and *JH* photometric observations are represented by error bars in the top panel while the solid line corresponds to the model fluxes at the parameters indicated in the figure; the hydrogen abundance is zero. The bottom panel shows the observed spectrum of OHDHS together with our predicted NaI D line profile.

Fig. 5.— Comparison of the best solutions for LHS 1402 under the assumption of a pure hydrogen composition (*dotted line*) and a mixed hydrogen/helium composition (*solid line*). Also shown are our broadband photometry (error bars) and optical spectrum from OHDHS. The latter suggests that LHS 1402 has a helium-rich composition rather than a pure hydrogen atmosphere.

Fig. 6.— Reduced proper motion diagram for the combined BRL and BLR samples (*open circles*) and the OHDHS sample (*filled symbols*). Filled circles and filled diamonds correspond to objects below and above $T_{\text{eff}} = 5000$ K, respectively. The objects labeled correspond to the halo white dwarf candidates identified by Liebert et al. (1989). Note that LHS 147 and LHS 542 are in common between the BRL and OHDHS samples. The two stars at the bottom are F351–50 (*left*) and WD 0351–564 (*right*).

Fig. 7.— Comparison of distances obtained from this study with those estimated by Salim et al. (2004). The discrepancy for LHS 4033 comes from the fact that we have used the trigonometric parallax information rather than assume a value of $\log g = 8.0$.

Fig. 8.— Distribution of tangential velocities (v_{tan}) with the V absolute magnitudes (M_V) for the white dwarfs from Table 2 (*filled circles*). The right axis indicates the temperature scale for $0.6 M_{\odot}$ white dwarf models. The trigonometric parallax sample of BLR is shown as well (*open circles*). The objects labeled are discussed in the text.

Fig. 9.— Masses of white dwarfs in the trigonometric parallax sample of BLR (*open symbols*), and halo white dwarf candidates from the OHDHS sample (*filled symbols*) as a function of effective temperature. Various symbols explained in the legend are used to differentiate values of the tangential velocities (in km s^{-1}). Objects with no trigonometric parallax measurements are shown at the bottom of the figure. Superposed are isochrones from white dwarf cooling sequences with thick hydrogen layers (*solid lines*); the isochrones are labeled in units of 10^9 years. Also shown are the corresponding isochrones with the main sequence lifetime taken into account (*dotted lines*).

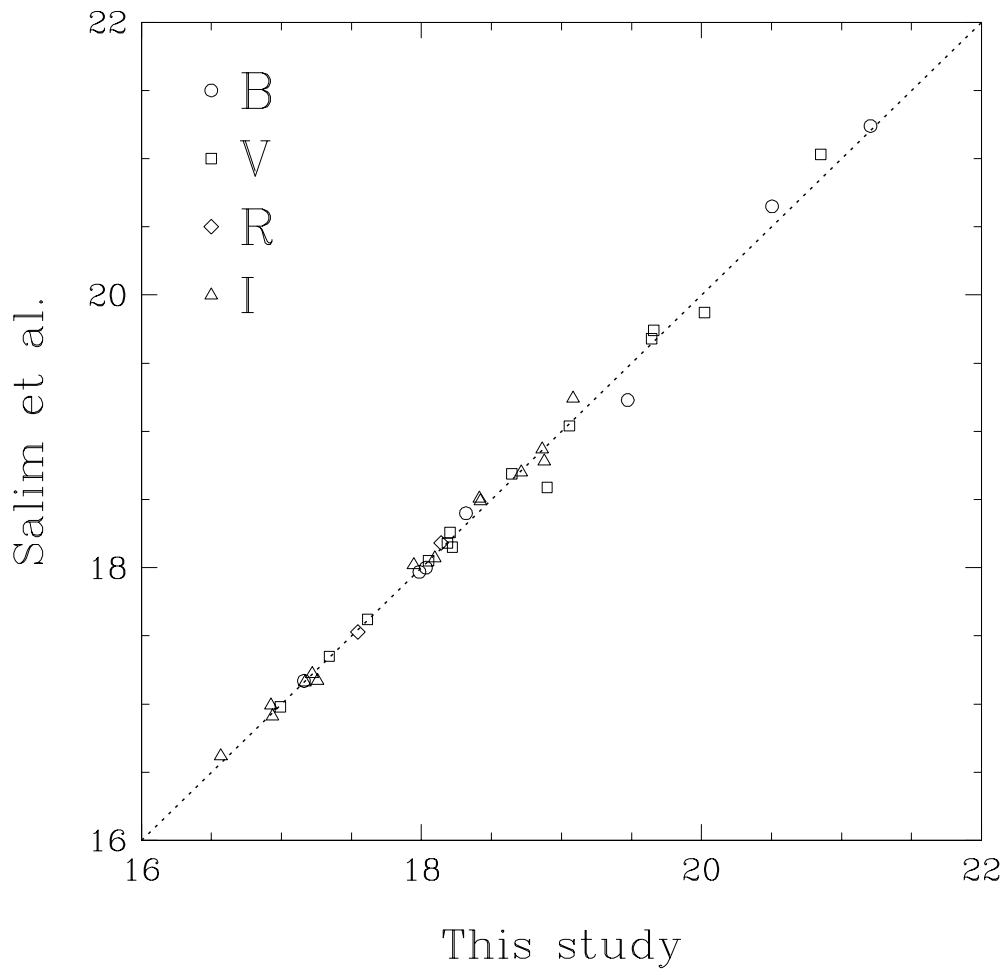


Figure 1

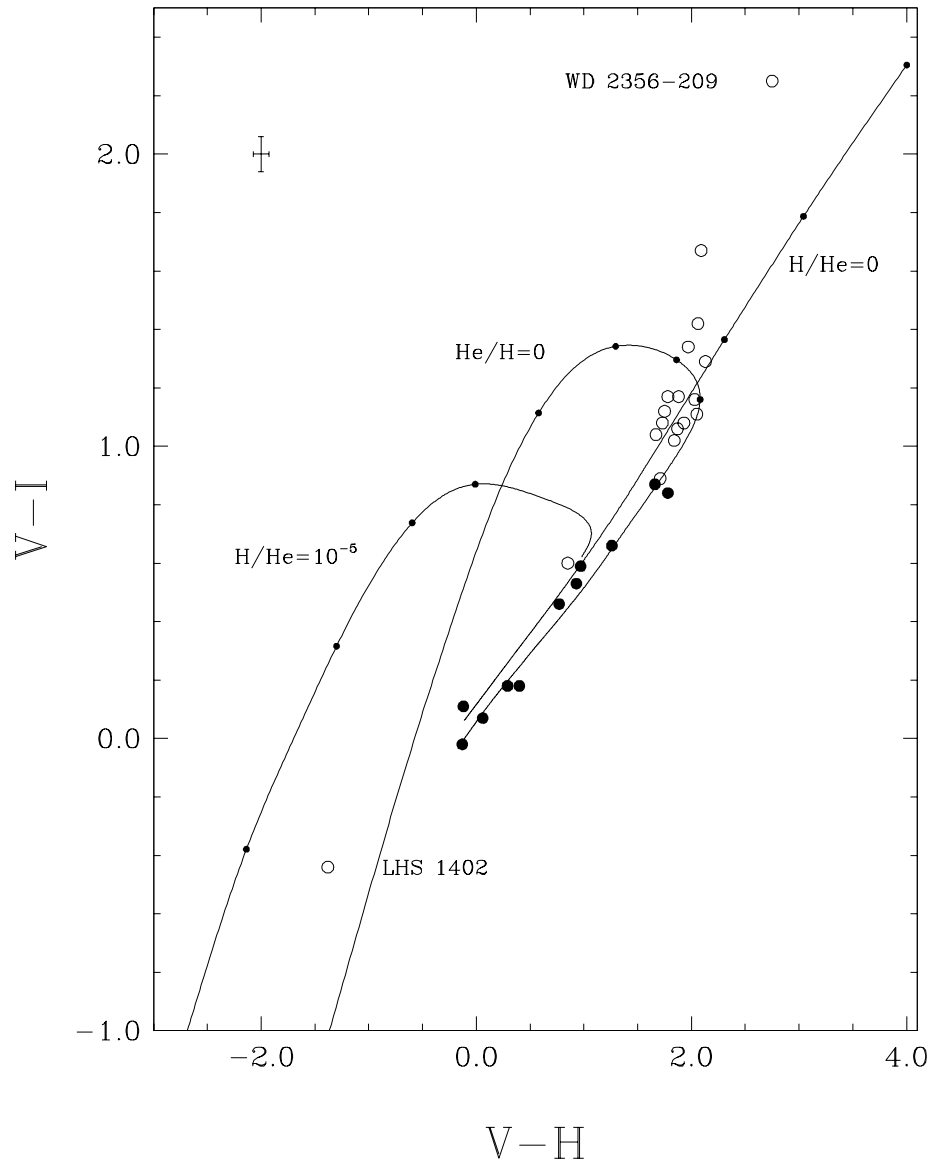


Figure 2

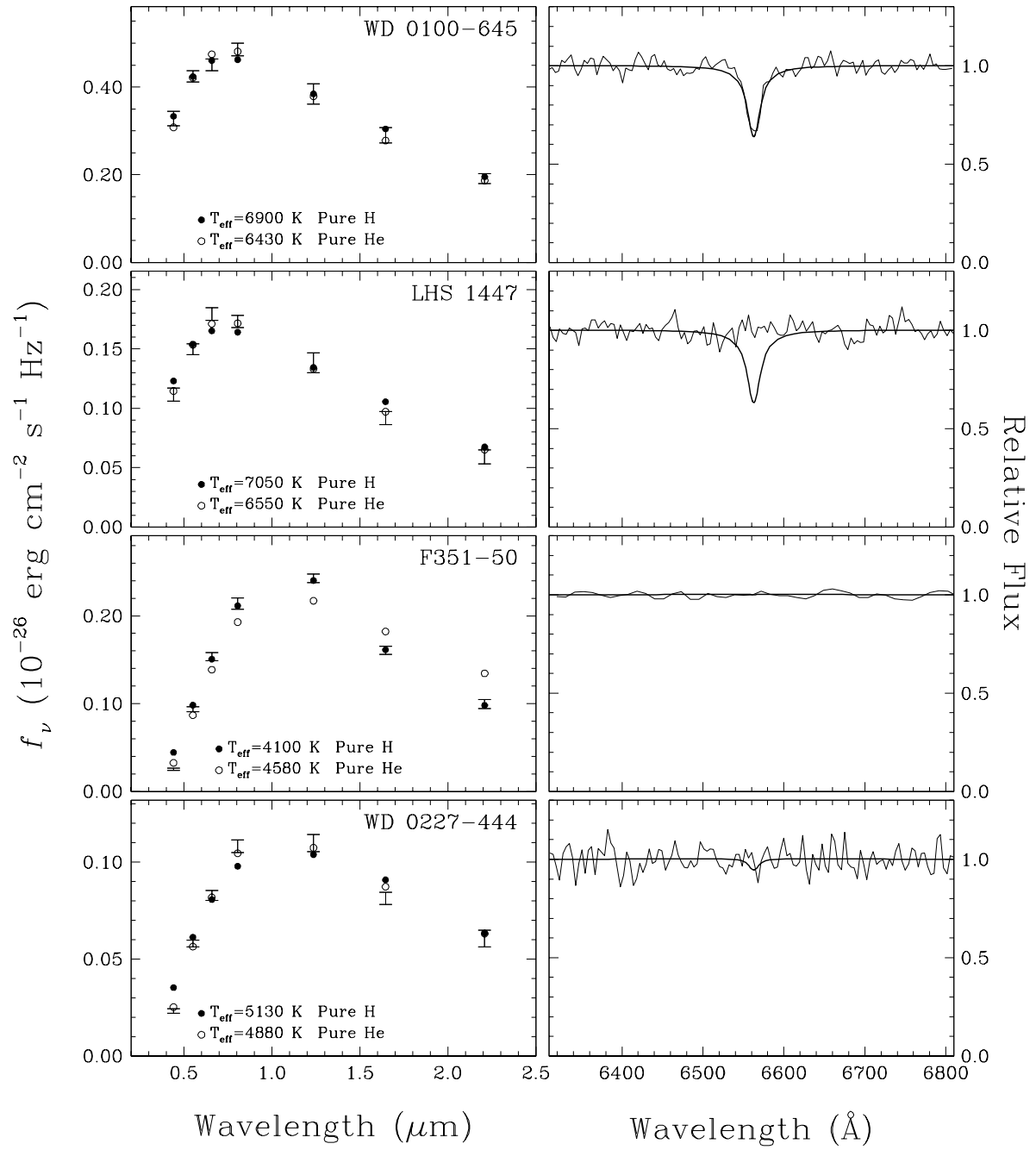


Figure 3

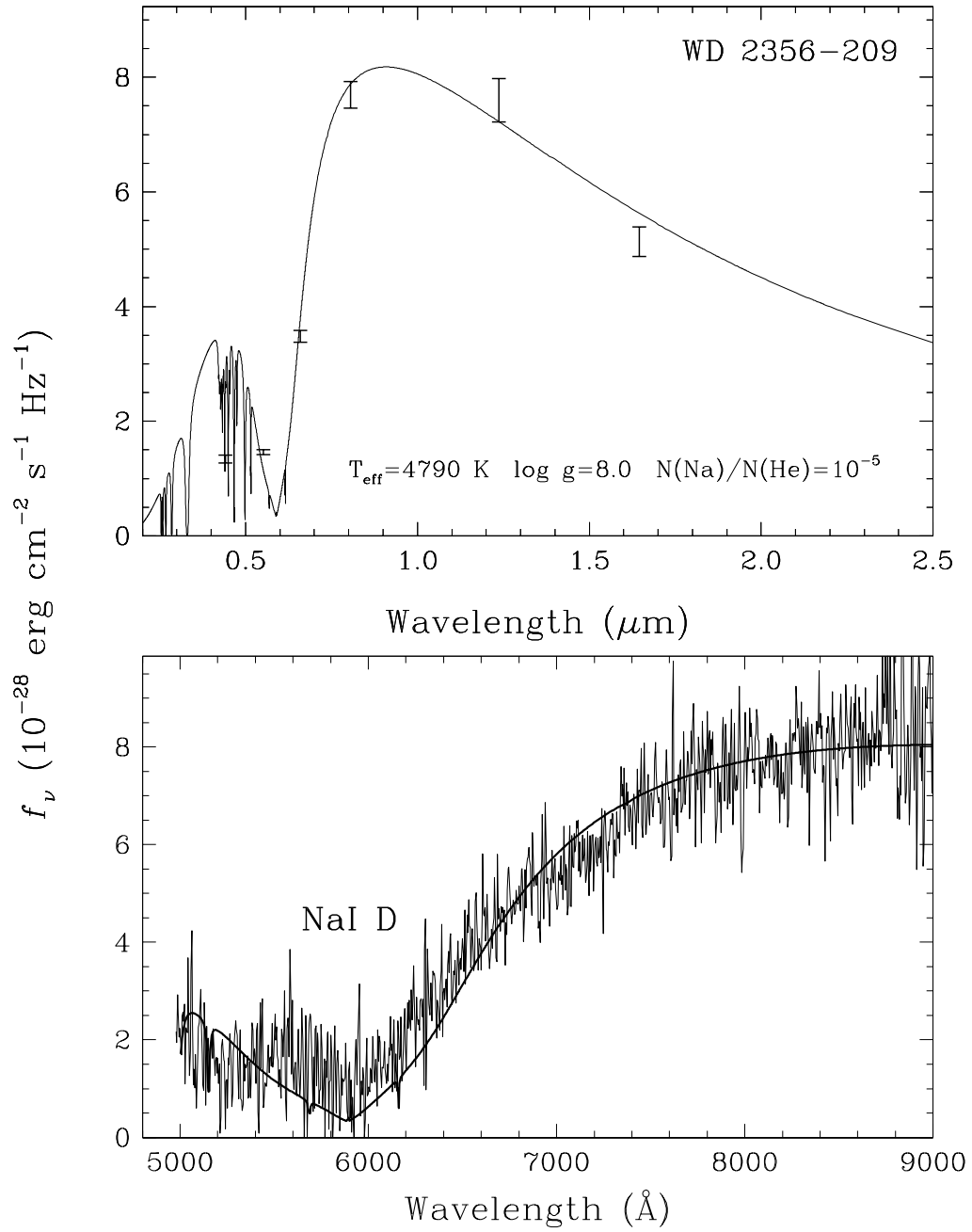


Figure 4

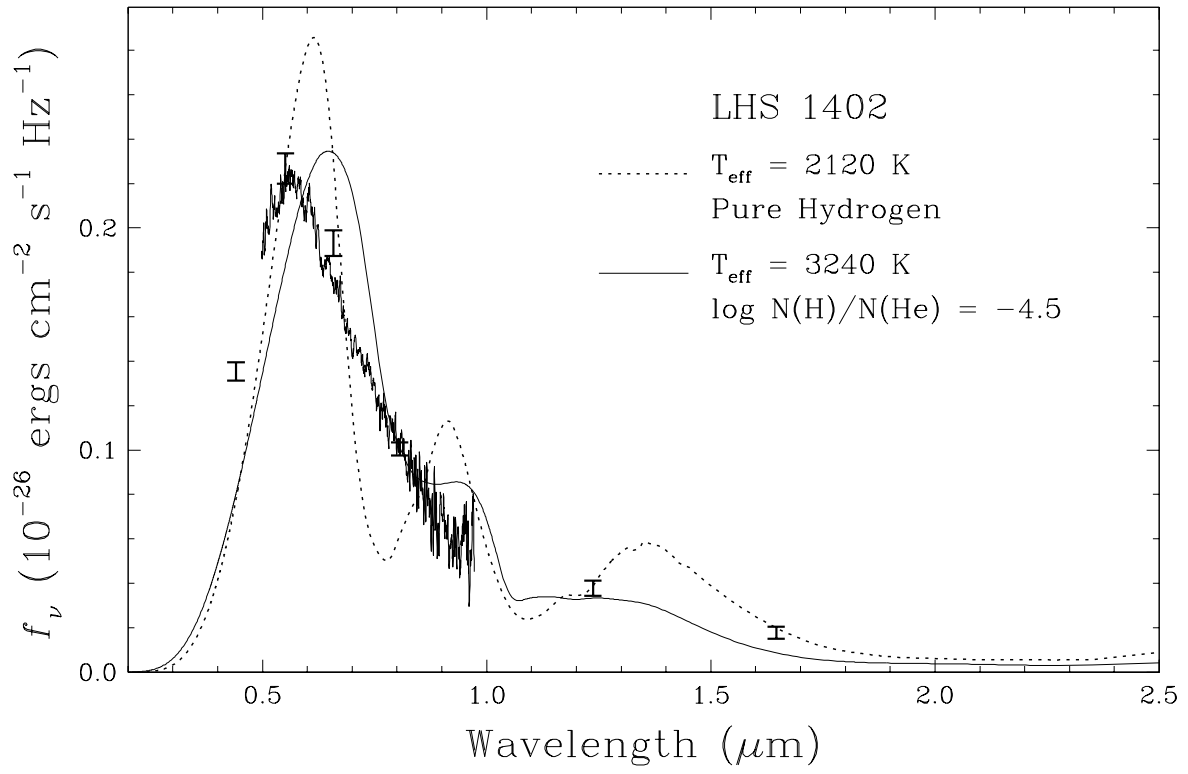


Figure 5

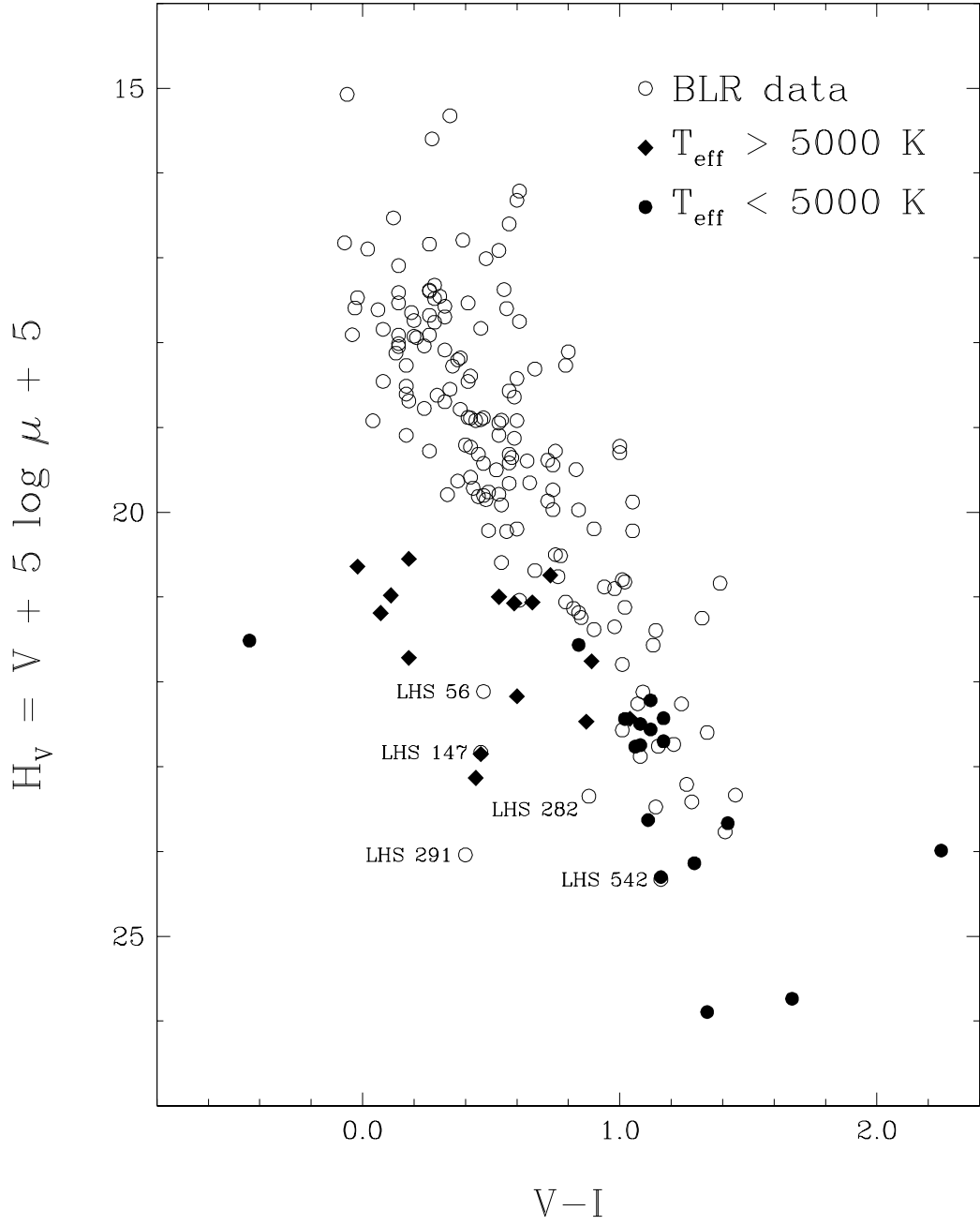


Figure 6

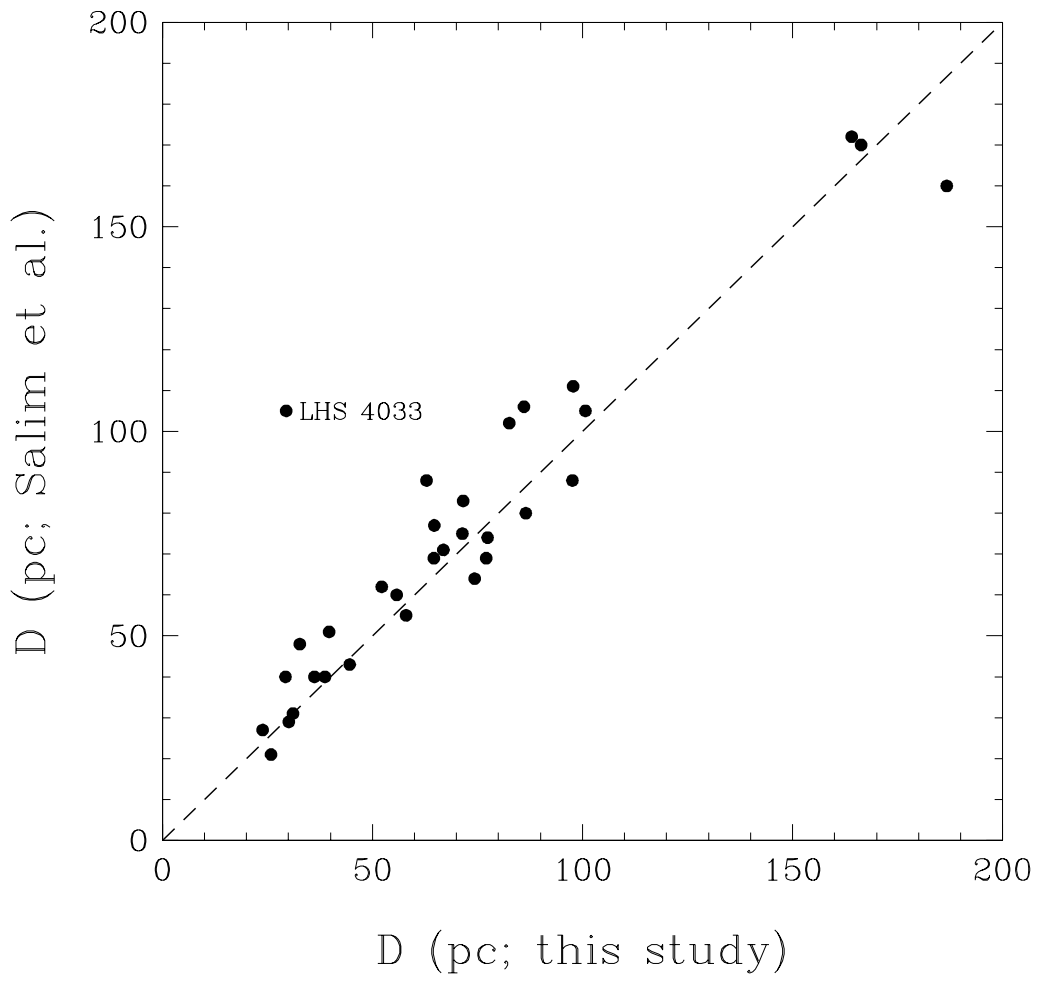


Figure 7

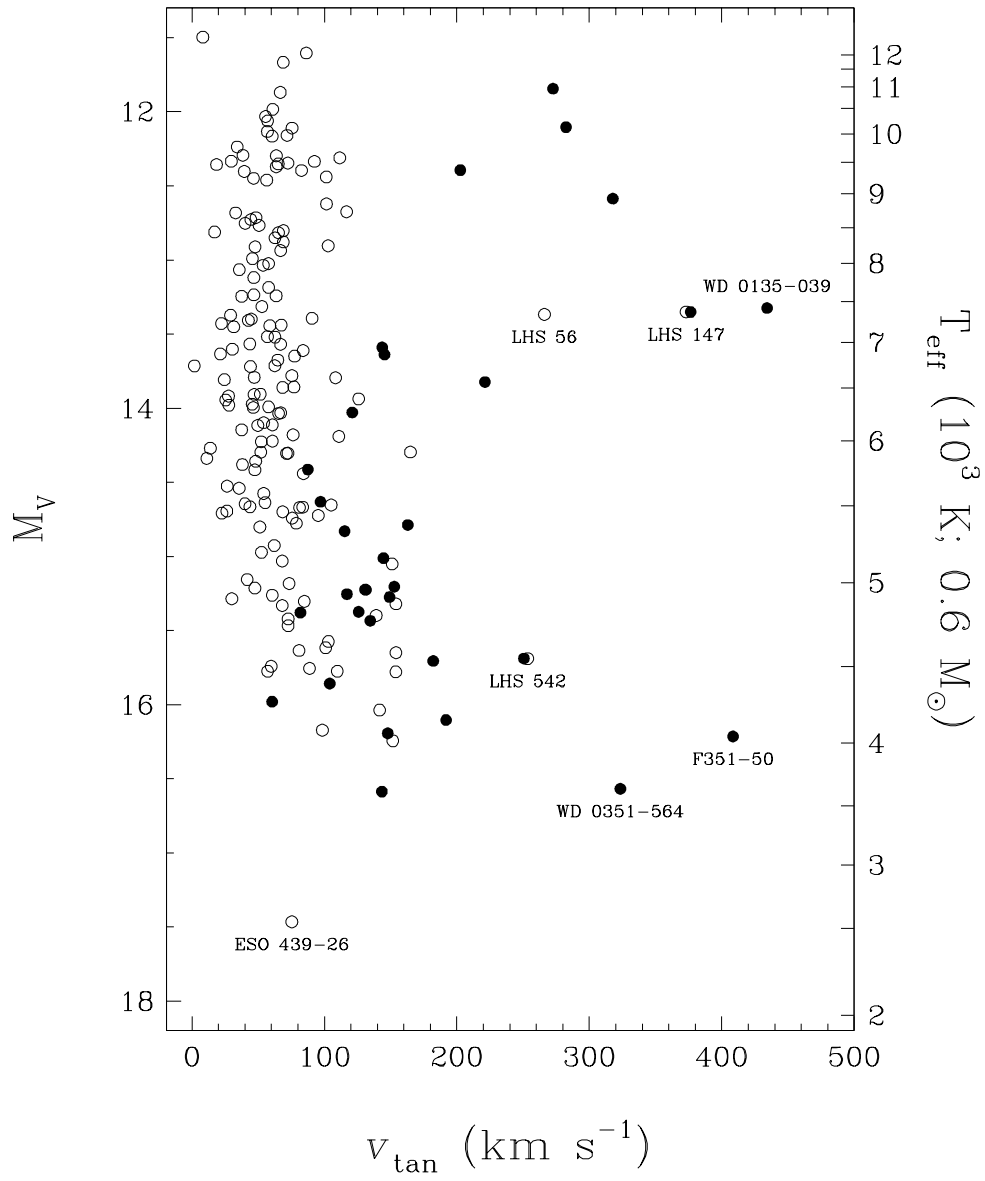


Figure 8

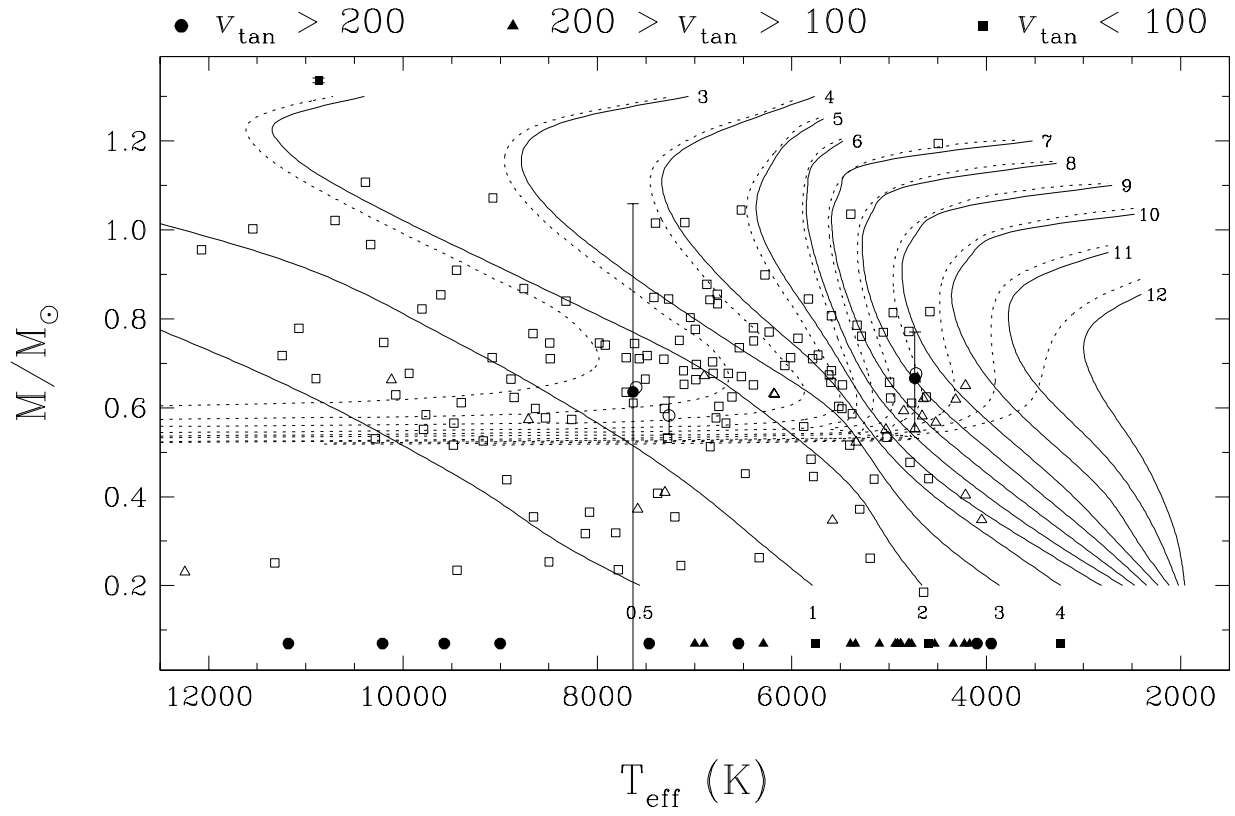


Figure 9